2014 IEEE International Conference on Robotics & Automation (ICRA)
Hong Kong Convention and Exhibition Center
May 31 - June 7, 2014. Hong Kong, China

Design and Control of a Robotic Wrist with Two Collocated Axes of Compliant Actuation

Cheng-Yu Chu, Jia-You Xu, and Chao-Chieh Lan, *Member*, IEEE

***Abstract*—It has been a challenge to design robots that possess intrinsic compliance, especially for robots that are required to achieve multi-DOF manipulation. Inspired by human limbs, robotic manipulators with internal compliance can perform high-quality force/torque control and better human-robot interaction. This paper presents a robotic wrist whose size, range, and torque output are comparable to those of a human wrist. To achieve two collocated and perpendicular axes of compliant actuation, two linear compliant couplers are proposed. Through slider crank and spherical mechanisms, the linear elasticity is converted to rotary elasticity to control the pitch and yaw torques at the same time. This new compact design realizes series elastic actuation in both axes without increasing size and complexity. Static and dynamic models of the compliant wrist are developed to analyze the motion. Through experiments of a prototype, the wrist is shown to achieve accurate and fast force/torque control. We expect this novel compliant wrist to serve as an alternative for applications involving human-robot interaction.**

Index Terms*—Wrist robots, force control, linear series elastic actuator, compliant mechanism.

I. Introduction

To meet the industrial need of high payload, accuracy, and speed, robotic manipulators have been traditionally designed to achieve maximum levels of torque output and stiffness. This requires stiff structural and transmission components. To reduce the overall weight, the manipulators often employ small electromagnetic motors with high gear reduction. When the manipulator applies a force to the environment, the force magnitude would be very sensitive to the displacement of the stiff manipulator. Together with the large friction force caused by high gear reduction, these two problems limit the manipulators from performing force control tasks in an accurate and fast manner. Improving the force control quality of industrial robots using high-end controllers or sensors, although possible, is usually costly.

Accurate force control and impact protection become more important with the increasing need of robots in a human-friendly environment. Unlike stiff industrial manipulators, human muscular systems are inherently compliant and can provide accurate force control. Inspired by nature, a compliant coupler can be placed between the gear box and output joint to emulate the muscular compliance. An actuator with a compliant coupler is also known as a series elastic actuator in the literature [1-2]. Multiple series elastic actuators can be used to form a compliant manipulator. With the compliant coupler, the output force is much less sensitive to the manipulator displacement. When a displacement sensor is used to measure the deformation of the compliant coupler, the original force control problem is then converted to a displacement control problem [1]. Hence accurate force control can be achieved more economically.

In addition to high-quality force control, the use of a compliant coupler can also significantly lower the impedance of the manipulator so that it is back-drivable and can reduce damage of unexpected human-robot collision. When properly designed and calibrated, the embedded displacement sensor can be used to obtain the output force. This avoids the use of external torque/force sensors which are usually more expensive. In addition to robotic manipulators, the concept of using compliant coupler has been applied to legged machines [3] and rehabilitation devices [4-6].

Adding a compliant coupler, on the other hand, will inevitably introduce oscillation under internal or external high-speed excitation. The position and force response speeds would be slower when the stiffness of the compliant coupler decreases. To mitigate these issues, the stiffness of the compliant element should be large enough. However, too large stiffness would in return degrade the force control quality and back-drivability. To improve the response of compliant manipulators at high speeds, a dual actuation approach has been proposed [7]. Another approach is to use variable stiffness coupler [8] so that the stiffness of the manipulator can adapt to different speeds. However, it is still a challenge to employ any additional components without making the manipulator too bulky.

From a mechanical perspective, the difficulty of achieving a compliant manipulator is that extra space within each joint is required to mount the compliant coupler and its associated displacement sensor. Hence the joint usually has to be large enough. Most existing compliant manipulators were designed by using rotary actuators with commercially available torsional springs or custom-made rotary compliant couplers [9-10]. This limits the applications to single-axis compliant joints that have comparable functions and sizes as human elbow or knee. Humanoid robots with intrinsic compliance have been proposed [11-13]. However, only one compliant axis is realized at each joint. As far as we know, manipulators having two or more collocated axes of compliant actuation have not been realized. In particular, manipulators with multiple perpendicularly intersecting axes of compliant actuation can realize multi-dimensional force regulation at the same location. They resemble complex human joints such as wrists or ankles and thus can be used to achieve an inherently compliant humanoid robot.

Aimed at achieving complex compliant actuation, this paper proposes a wrist manipulator with two collocated axes of compliant actuation. In what follows, we first present the design of the compliant wrist in Sec. II. The kinematic and

This work was supported in part by the National Science Council of Taiwan (with Project No. NSC 101-2221-E-006-027).

C.-Y. Chu, J.-Y. Xu, and C.-C. Lan are with the Department of Mechanical Engineering, National Cheng Kung University, No. 1, University Rd., Tainan, Taiwan. (corresponding author e-mail: cclan@mail.ncku.edu.tw).

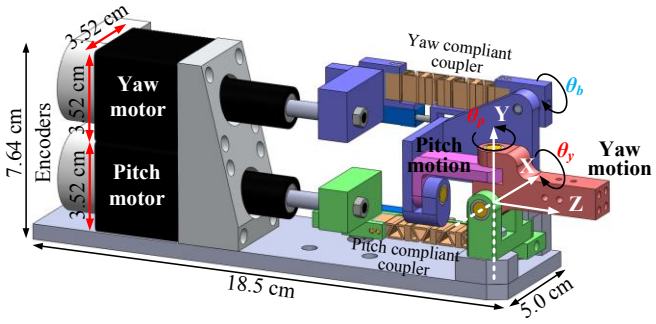

Fig. 1 The proposed compliant wrist

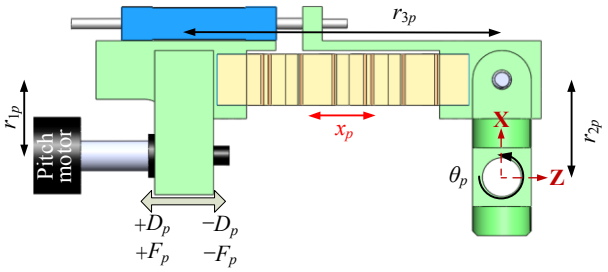

Fig. 2 The pitch mechanism

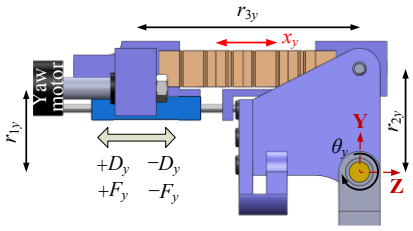

Fig. 3 The yaw mechanism

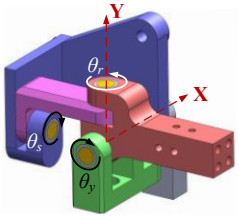

Fig. 4 The 5R spherical mechanism

static models are developed in Sec. III. The design of the compliant couplers is presented in Sec. IV. This is followed by the dynamic analysis to verify the performance of the wrist. Finally, control experiments of a prototype are presented.

II. Design of the Compliant Wrist

Fig. 1 shows the CAD model of the proposed compliant wrist. The wrist is actuated by two identical linear step motors. The bottom pitch motor actuates the pitch mechanism and the top yaw motor actuates the yaw mechanism. The pitch and yaw mechanisms are connected to the 5R spherical mechanism to generate two output axes of rotation that perpendicularly intersect at the origin of global frame **XYZ**. The pitch motion rotates θ_p around the **Y** and yaw motion rotates θ_y around the **X** axis. Without interference, the wrist can provide a pitch range θ_p from −59.12° to 45.09° and a yaw range θ_y from −45.77° to 54.78°. These correspond to motor input displacements from −1.79 to 1.39 cm. The encoders behind the motors record the motor displacements. The wrist has an end rod that can be extended to mount an end-effector.

Figs. 2 and 3 show the pitch and yaw compliant mechanisms at their neutral positions. Each one is a slider crank mechanism with a compliant coupler. The link dimensions of the pitch and yaw mechanisms are similar. The pitch is placed parallel to the **XZ** plane and the yaw is placed parallel to the **YZ** plane. The deformation of each coupler is measured by using a potentiometer (BOURNS® 3048L-5-502) with measureable stroke up to 12.7 mm. In Fig. 2, a displacement D_p from the pitch motor creates a pitch angle θ_p. In Fig. 3, a displacement D_y from the yaw motor creates an input yaw angle θ_b. Through the 5R spherical mechanism shown in Fig. 4, the input yaw angle is transmitted to the output yaw angle θ_y. Table 1 lists the dimensions of the wrist. The undeformed lengths of the pitch and yaw couplers are denoted as r_{3p} and r_{3y}. The stiffnesses of the couplers are denoted as k_p and k_y. When given axial deformations x_p and x_y, the corresponding pitch force f_p and yaw force f_y are generated.

Table 1 Wrist dimensions

Pitch mechanism	Yaw mechanism
r_{1p} = 2 cm; r_{2p} = 2 cm;	r_{1y} = 3 cm; r_{2y} = 3 cm;
r_{3p} = 6.5 cm;	r_{3y} = 6.5 cm;
D_p = −1.79 to 1.39 cm	D_y = −1.79 to 1.39 cm
F_p = –222 to 222 N	F_y = –222 to 222 N

The overall size of the wrist is 18.5×7.64×5.0 cm^3. Each motor can provide a force up to 222 N. At the neutral position, the pitch and yaw torque can reach up to ±4.44 Nm. The wrist was designed to emulate the size, workspace, and torque density of a normal human wrist. The proposed compliant wrist is different from others in that the rotational compliance is achieved by the transmitted linear compliance provided by the two compliant couplers. The two couplers make it possible to fit in the restricted space in the wrist without increasing its size. The compliant couplers can be readily replaced by rigid couplers if rigidity becomes the primary concern.

III. Kinematic and Static Analyses

The D_p-θ_p and D_y-θ_b relations can be obtained by solving the following equations.

$$D_p = -r_{3p} + r_{2p}S_p + [(r_{3p} + x_p)^2 - (r_{2p} - r_{2p}C_p)^2]^{1/2} \quad (1)$$

$$D_y = -r_{3y} - r_{2y}S_b + [(r_{3y} + x_y)^2 - (r_{2y} - r_{2y}C_b)^2]^{1/2} \quad (2)$$

where S and C are the sine and cosine functions. Within the workspace, the D_p-θ_p and D_y-θ_b relations are quite linear. A positive D_p results in a positive θ_p while a positive D_y results in a negative θ_b. The output yaw angle is related to the pitch angle and input yaw angle by

$$\theta_y = T^{-1}(T_b / C_p) \quad (3)$$

where T is the tangent function. For the special case where θ_p = 0, the output and input yaw angles are identical. For other values of θ_p, the magnitude of the output yaw angle will be increasingly larger than the magnitude of the input yaw angle. Based on Eq. (3), the feasible domain of the output pitch and yaw angles is obtained as shown in Fig. 5. The difference between θ_b and θ_y is largest when θ_p = −60° and θ_b = ±30°, at which θ_y = ±49.11° and the difference is 19.11°.

Fig. 5 shows the skeleton diagram of the wrist. By using free-body analyses, the input pitch torque τ_a is related to the pitch motor force F_p by

$$\tau_a = r_{2p}(C_{32} / C_{34})F_p$$

$$\text{where} \quad \theta_{32} = \sin^{-1}[(r_{2p}C_p - r_{1p}) / r_{3p}] - \theta_p \quad (4)$$

$$\text{and} \quad \theta_{34} = \sin^{-1}[(r_{2p}C_p - r_{1p}) / r_{3p}]$$

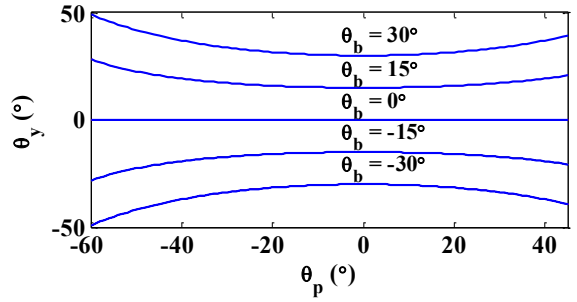

Fig. 5 Feasible domain of the pitch and yaw angles

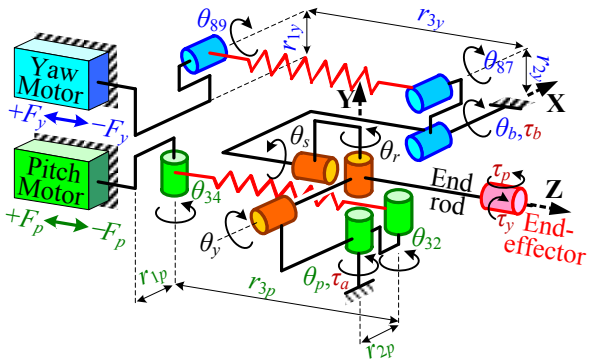

Fig. 6 Skeleton diagram of the compliant wrist

Likewise, the input yaw torque τ_b is related to the yaw motor force F_y by

$$\tau_b = -r_{2y}(C_{87}/C_{89})F_y$$

$$\text{where } \theta_{87} = \sin^{-1}[(r_{1y} - r_{2y}C_b)/r_{3y}] - \theta_b \quad (5)$$

$$\text{and } \theta_{89} = \sin^{-1}[(r_{1y} - r_{2y}C_b)/r_{3y}]$$

As shown in Fig. 6, the input pitch and yaw torques are further transmitted to the output pitch and yaw torques (τ_p and τ_y) on the end rod through the spherical mechanism. The output pitch and yaw torques are to balance with any external torque applied on the end-effector. The following equation is used to relate the output torques to the input torques.

$$\begin{bmatrix}\tau_p\\ \tau_y\end{bmatrix} = \begin{bmatrix}1/C_y & -S_{2b}T_p/2C_y\\ 0 & C_b^2C_p + S_b^2/C_p\end{bmatrix}\begin{bmatrix}\tau_a\\ \tau_b\end{bmatrix} \quad (6)$$

It can be shown that θ_{34} and θ_{89} are both very small (less than 4° in the full range). Hence Eqs. (4~5) can be simplified as follows.

$$\tau_a = r_{2p}C_pF_p = r_{2p}C_pk_px_p$$
$$\tau_b = -r_{2y}C_bF_y = -r_{2y}C_bk_yx_y \quad (7)$$

Once the stiffness and elongation of the couplers are known, they can be used to obtained the input and output torques.

IV. Design of the Compliant Couplers

4.1 Design

The compliant wrist in Fig. 1 relies on two compliant couplers to obtain the elastic motion at the output. Each coupler needs to provide the required stiffness in the limited space (6.5 cm long) between the motor and the spherical mechanism. To reduce the complexity of using a parallel placed guide rail, the coupler must also be able to resist lateral deformation during loading operations.

Commercially available coil springs of the same stiffness are too large and cannot meet the space requirements. We propose a custom-made planar spring to serve as the compliant coupler. Fig. 7(a) shows the CAD model of the coupler. The size of the coupler is 51.5×10.5×6 mm^3. It consists of four serially connected cells when viewed in the XZ plane. The cells are connected in a way that neighboring cells are flipped vertically. Since the planar spring is not symmetric, the flip can be used to reduce the parasitic reaction forces in the X direction. Following the method in Refs. [14-15], the shape of each cell is numerically optimized in order to achieve the required stiffness while maintaining minimal stress. Fig. 7(b) shows the assembled view of the yaw coupler. To increase the deformation ability, we use Titanium (6Al-4V) as the material. Titanium has a very high yield stress to elastic modulus ratio. Its density is only slightly larger than Aluminum alloy. The coupler is fabricated by using wire electrical-discharge machining. Pins with diameter of 2 mm are press-fitted into the four holes on the two sides so the coupler is rigidly connected to the neighboring aluminum connectors and joints.

The pitch and yaw couplers have the same dimension and stiffness. To ensure accurate force sensing, the stiffness is designed such that a noticeable displacement of 1.5 mm can be measured in the potentiometer when the motor force is 196.875 N. This equals to a stiffness of 131.25 N/mm. To achieve this stiffness, the corresponding in-plane thickness of the cells is 0.77 mm. The in-plane thickness can be changed to meet other stiffness requirements without changing other dimensions of the coupler.

This planar spring design offers several unique advantages to be an ideal compliant coupler:

(i) The compliant coupler needs to provide stiffness in both tensile and compressive directions. Commercially available compression springs cannot be directly used in the tensile direction because they have no hooks at the two ends. The proposed planar spring, on the other hand, has built-in connectors at the two ends and hence can be simultaneously used for compression and tension.

(ii) The planar springs can be designed to have a thin cross-section. They can fit in the limited space and make the wrist more compact.

(iii) Unlike coil springs that are flexible in all directions, the planar spring can be cleverly designed to have relatively large bending stiffness so as to avoid buckling.

(iv) Although a potentiometer is used to measure the spring deformation, planar springs can be designed to have flat surfaces for attaching strain gauges. Using strain gauges to measure deformation can further minimize the size and simplify the design.

The proposed coupler (denoted as Case B) shown in Fig. 7 was originated from a trial design (denoted as Case A) shown in Fig. 8. Case A is also made of multiple cells. Each cell shape is the same as that in Case B. Unlike Case B, the cells in Case A were arranged such that they are symmetric in the YZ plane. The stiffnesses of both cases are the same. Since the rotational axes of the two neighboring joints are normal to the YZ plane, this facilitates the fabrication of the coupler and its neighboring connectors from one piece of material. As for Case B, the coupler and the connectors have to be separately fabricated and then rigidly joined by using pins.

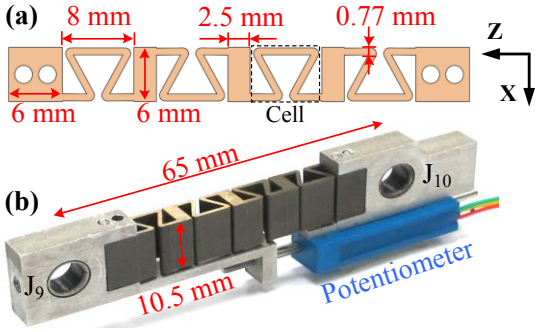

Fig. 7 (a) CAD model of the compliant coupler (b) Assembled view

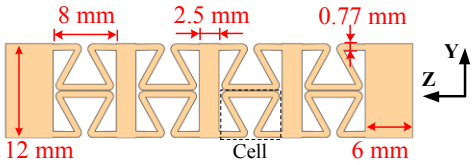

Fig. 8 A trial design of the coupler (Case A)

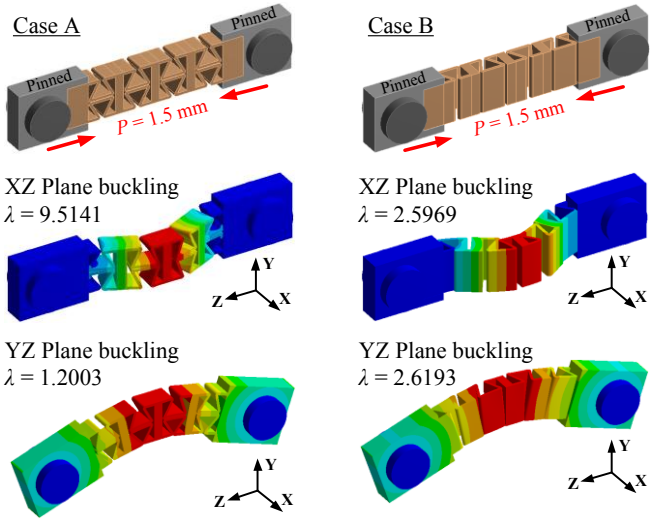

Fig. 9 Buckling analysis of the couplers

Although Case B requires more fabrication and assembly, it is preferable because of its superior ability to resist buckling. A linear static buckling analysis was performed in ANSYS® to compare the buckling load of the two cases. A displacement load of $P = 1.5$ mm was given to each coupler. The two ends of the coupler are pinned-pinned in order to comply with its motion in the slider crank mechanism. The critical buckling load P_{cr} was then obtained. Fig. 9 shows the buckling deformation in the **XZ** and **YZ** planes, where λ is the load multiplier such that $P_{cr}/P = \lambda$. The larger the value of λ, the more the coupler can resist buckling. Although Case A has a very large λ in the **XZ** plane, its λ in the **YZ** plane is very small. Hence buckling in the **YZ** plane will first occur. As for Case B, the multipliers are moderate in both planes. Thus the coupler in Case B can resist a larger load before buckling.

4.2 Comparison of Simulation and Experiment Results

The solid model of the planar spring was imported into ANSYS® for further evaluation. Fig. 10 shows the stress diagrams of compression and tension. The maximum equivalent stress is 461.89 MPa when an extensional displacement of 1.5 mm is given. The maximum equivalent stress is about half of the yield stress (828 MPa) of the material.

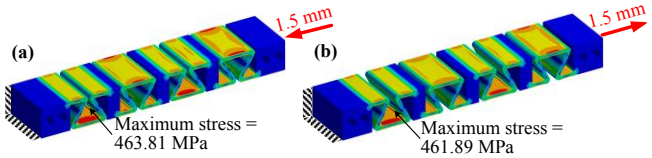

Fig. 10 (a) Compression (b) Extension

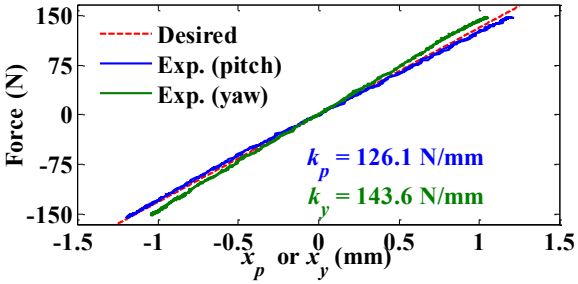

Fig. 11 Experimental force-displacement curves

A static experiment was performed to measure the stiffness of the coupler shown in Fig. 7(b). In the experiment, a closed-loop sinusoidal force command of 1 Hz and 150 N amplitude was given. The actual force was recorded by a force sensor and the coupler displacement by the potentiometer. Fig. 11 shows the experimental force-displacement curves of the pitch and yaw couplers. Both curves are very linear with almost no hysteresis. The stiffnesses are 126.1 and 143.6 N/mm, respectively. They are slightly different from the desired stiffness of 131.25 N/mm, primarily due to the machining and material imperfections.

V. Dynamics and Control

5.1 Dynamic model

We consider the case where an end-effector with mass m is attached on the end rod with distance r from the center of the wrist. Gravity is assumed to act in the negative **Y** direction. The inertia effects of the links and couplers are much smaller than the mass of the end-effector and hence are ignored. The kinetic energy T and potential energy V of the wrist can be derived as

$$T = \tfrac{1}{2}M_m\dot{D}_p^2 + \tfrac{1}{2}M_m\dot{D}_y^2 + \tfrac{1}{2}mr^2\dot{\theta}_y^2 + \tfrac{1}{2}mr^2\dot{\theta}_p^2\cos^2\theta_y;$$
$$V = \tfrac{1}{2}k_p x_p^2 + \tfrac{1}{2}k_y x_y^2 - mgr\sin\theta_y \quad (8)$$

where M_m is the equivalent mass of the rotor with respect to the leadscrew axis. With aid of Eqs. (1~3) to convert D_p and D_y to θ_p and θ_y, the Lagrange's equations for the wrist can be derived. The equations are quite lengthy but their general form can be written as follows.

$$\mathbf{M}(\mathbf{q},\dot{\mathbf{q}})\ddot{\mathbf{q}} + \mathbf{f}(\mathbf{q},\dot{\mathbf{q}}) + \mathbf{g}(\mathbf{q}) = \mathbf{Q} \quad (9)$$

where $\mathbf{q} = [\theta_p\ \theta_y\ x_p\ x_y]$ is the vector of dependent variables, **M** is the inertia matrix, **f** is the velocity coupling vector, **g** is the gravitational vector, and **Q** is the vector of generalized forces. Each generalized force is a function of the motor forces F_p and F_y. Considering the pitch motor as an illustration, the feedback motor force is given as follows to control the pitch angle θ_p to meet the reference θ_{pr}.

$$F_p = \alpha_p(\theta_{pr} - \theta_p) - \beta_p\dot{\theta}_p - \gamma_p\dot{x}_p - h_p x_p + g_p(\theta_p,\theta_y) \quad (10)$$

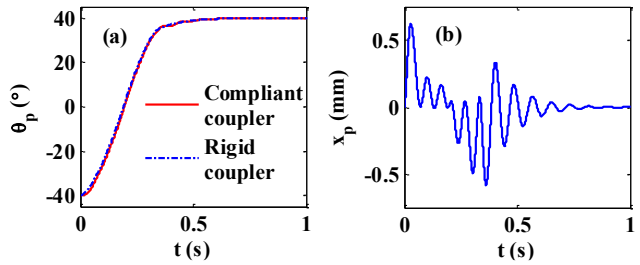

Fig. 12 (a) Step response of the pitch motion (b) Deformation of the pitch coupler

where α_p and β_p are the proportional and derivative gains for the response of θ_p, h_p and γ_p are the proportional and derivative gains for the response of x_p. The function g_p is used to compensate for gravity. The motor dynamics can be extensively found in the literature (e.g., Ref. [16]). Considering the pitch motor, its governing equations are

$$di_a / dt = [v_a - Ri_a + K_m \dot{\theta}_m \sin(N_r \theta_m)] / L \quad (11a)$$

$$di_b / dt = [v_b - Ri_b - K_m \dot{\theta}_m \cos(N_r \theta_m)] / L \quad (11b)$$

$$F_p = \alpha K_m [-i_a \sin(N_r \theta_m) + i_b \cos(N_r \theta_m)] \quad (11c)$$

where v_a, v_b and i_a, i_b are the voltages and currents in phases A and B, respectively. The angle θ_m is the rotation of the rotor, K_m is the motor torque constant, R is the resistance of the phase winding, L is the inductance of the phase winding, N_r is the number of rotor teeth, and α is the amplification factor of the leadscrew. Once i_a and i_b are obtained in Eqs. (11a) and (11b), they can be inserted into Eq. (11c) to compute the pitch motor force F_p. To meet practical constraints, a saturation voltage of ±10 V was given to v_a and v_b.

Table 2 Dynamic and control parameters of the wrist

m = 1 kg	M_m = 18.187 kg	α_p = 1018.59 N
r = 0.12 m	K_m = 0.141 Nm/A	β_p = 120.01 Ns
g = 9.81 m/s^2	R = 12.544 Ω	γ_p = 3000 Ns/m
α = 2595.36 m^{-1}	L = 18.063 mH	h_p = 10000 N/m
N_r = 50		

By using Eqs. (9~11), a simulation is performed in MATLAB to study the dynamics of the wrist. The simulation parameters are listed in Table 2. Specifically, a considerable mass of 1 kg is used to represent the end-effector load. The controller gains for the pitch motor are tuned such that a maximum speed can be generated without overshoot. The motor parameters K_m, R, and L are experimentally determined. Fig. 12(a) shows the step response from -40° to 40°. Two cases are tested, the first is with the compliant coupler and the second is with a rigid couple where k_p is infinity. The same controller gains are used, except that there are no γ_p and h_p terms for the case with a rigid coupler. As can be seen, the response of using the compliant coupler is almost the same as that of using the rigid coupler. By using the control law in Eq. (10), the inherent compliance has negligible effect on the pitch angle control. The rise time for both cases is 0.254 sec. Fig. 12(b) shows the pitch coupler deformation with respect to time. The maximum deformation is about 0.5 mm.

Fig. 13 shows the frequency response of the pitch motion where a sinusoidal position signal with frequency of 1.49 Hz and amplitude of 40° is given for θ_{pr}. Same as that in Fig. 12(a), the response is almost the same as that of using a rigid coupler. The responded amplitude is 28.23°, indicating that the bandwidth of the pitch motion is about 1.49 Hz. The bandwidth is limited by controller gains and voltage saturation. The control law and dynamics of the yaw motion can be obtained in a similar fashion. The response speed is expected to be slower due to the presence of gravity load.

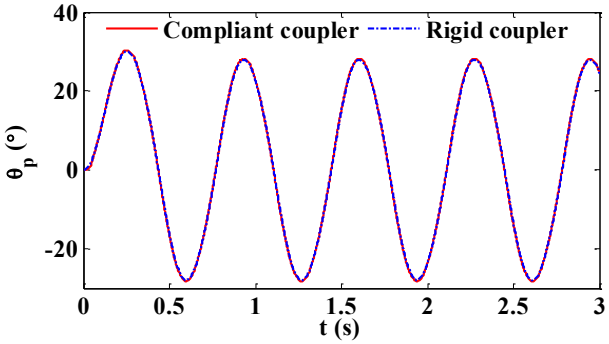

Fig. 13 Frequency response of the pitch motion

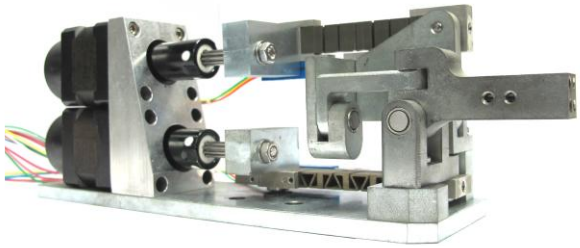
Fig. 14 Wrist prototype

5.2 Prototype

Fig. 14 shows a wrist prototype fabricated based on the CAD model shown in Fig. 1. The links and pins are made of carbon steel to ensure structural rigidity. Including the bottom plate, the wrist weighs about 1.38 kg, of which each motor weighs 220 g.

5.3 Force/Torque control experiments

Eqs. (9~11) can be simplified to simulate the force control response of the wrist. As an illustration, we consider a case where the end rod is held fixed at $\theta_p = \theta_y = 0$. The pitch mechanism is to follow a reference force f_{pr}, i.e., the output pitch torque is required to follow a reference torque $r_{2p} \times f_{pr}$. The following control law is proposed for the pitch force.

$$\text{If } |f_{pr} - f_p| \geq 2,\ F_p = f_p + \alpha_p (f_{pr} - f_p) - \beta_p \dot{f}_p + f_{cp}$$
$$\text{else } F_p = f_p \quad (12)$$

In Eq. (12), a 2-N threshold is used for F_p since forces below 2 N is not controllable due to the voltage noise of the potentiometer. When $|f_{pr} - f_p| \geq 2$, the first term of F_p in Eq. (12) is used to maintain the static equilibrium position when the required force value is satisfied. The second and third terms are the PD control inputs. Since the unavoidable leadscrew clearance would cause oscillation during small force control, the proportional gain is tuned to be a function of the measured force f_p. Based on α_p, the derivative gain β_p is further tuned to achieve exponential stability.

$$\text{If } |f_p| < 50 \text{ N},\ \alpha_p = 1;\ \text{else } \alpha_p = 1 + 0.5(|f_p| - 50) \quad (13a)$$

$$\beta_p = \sqrt{4 M_m \alpha_p / k_p} \quad (13b)$$

Thus a large α_p is used to accelerate the response at a large force magnitude and a small α_p is used to avoid the

clearance-induced oscillation at a small force magnitude. The fourth term in Eq. (12) is used to compensate the friction force in the leadscrew, where f_{cp} increases with the magnitude of f_p.

$$f_{cp} = \text{sign}(f_{pr} - f_p) \times (10 + 0.7 \mid f_p \mid) \quad (14)$$

The force control law for the yaw mechanism can be derived in a similar fashion.

At $\theta_p = 0$, the pitch force control experiment can be carried out in an equivalent configuration where the crank is removed and the pitch motor is aligned with the pitch coupler. Fig. 15 shows the experimental setup. Two load cells (Futek LSB 200, maximum 445 N) were used to measure the pitch force f_p. The proposed control law was implemented in NI cRIO 9076 with a sampling frequency of 50 kHz. Fig. 16 shows the force step response. For the 100-N step response in Fig. 16(a), the rise time is 0.046 sec. Except for the slight variation at $f_p = 50$ and −50 N, the experiment results match well with the simulation. For the 300-N step response in Fig. 16(b), the rise time is 0.088 sec. The actual response is slower than the simulation. This is primarily due to the un-modeled friction force in the pitch motor.

Fig. 17 shows the frequency response of the pitch force. The same control law is used in the experiment to track a sinusoidal force reference with amplitude of 50 N (small force) and 150 N (large force). The bandwidth of the small-force response in Fig. 17(a) is 17 Hz while the bandwidth of the large-force response in Fig. 17(b) is 6.5 Hz. Simulation results are compared in both subfigures. The simulation is conducted by using the same control law in Eq. (12) without considering friction. In the large-force response where the frictional effect is more obvious, the experimental response can be seen to be slower than the simulation. The results of the 150-N force response indicate that the wrist can provide a pitch or yaw torque of ±3 Nm with bandwidth of 6.5 Hz.

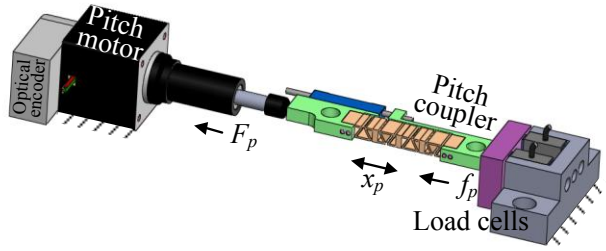

Fig. 15 Experimental setup of force control

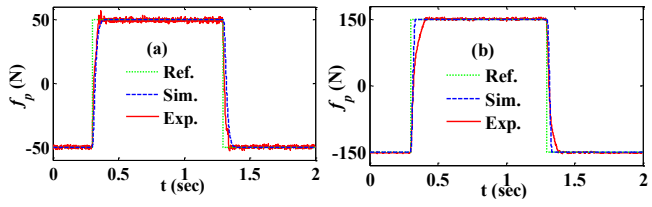

Fig. 16 (a) Small-force response (b) Large-force response

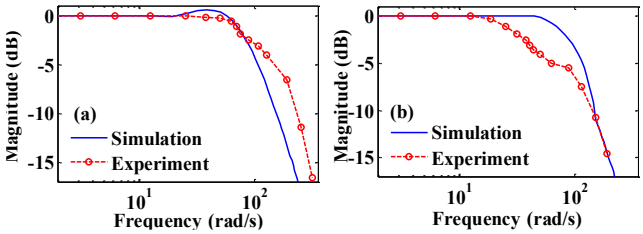

Fig. 17 (a) Small-force response (b) Large-force response

VI. Conclusions

This paper has presented the design, analysis, and experiment of a compliant wrist manipulator. The wrist includes two linear step motors, two slider crank mechanisms, and a spherical mechanism to achieve pitch and yaw motion whose displacement and torque are comparable to those of a human wrist. To obtain intrinsic compliance and better force control quality, two compliant linear couplers were inserted between the motors and linkages. The sizes of the couplers and their potentiometers have been specifically designed to achieve the required stiffness in a limited space that must resemble the appearance of a human wrist. Without introducing much complexity, the pitch and yaw compliant motions can be simultaneously realized. Torque-control experiments showed that a torque amplitude of 3 Nm can be achieved with a bandwidth of 6.5 Hz. We expect the proposed wrist can be applied to the design of humanoid robot arms and rehabilitation devices that require high force control quality.

References

[1] G. A. Pratt, M. M. Williamson, 1995, "Series elastic actuators," IEEE/RSJ Int. Conf. Intell. Robots Syst., 1, 399-406.

[2] J. Pratt, B. Krupp, C. Morse, 2002, "Series elastic actuators for high fidelity force control," Int. J. Ind. Robot, 29(3), 234-241.

[3] D. W. Robinson, J. E. Pratt, D. J. Paluska, G. A. Pratt, 1999, "Series elastic actuator development for a biomimetic walking robot," IEEE/ASME Int. Conf. Adv. Intell. Mechatron., 561-568.

[4] J. E. Pratt, B. T. Krupp, C. J. Morse, S. H. Collins, 2004, "The RoboKnee: an exoskeleton for enhancing strength and endurance during walking," IEEE ICRA, 3, 2430-2435.

[5] J. F. Veneman, R. Ekkelenkamp, R. Kruidhof, F. C. van der Helm, H. van der Kooij, 2006, "A series elastic-and bowden-cable-based actuation system for use as torque actuator in exoskeleton-type robots," Int. J. Robot. Res., 25(3), 261-281.

[6] K. Kong, J. Bae, M. Tomizuka, 2009, "Control of rotary series elastic actuator for ideal force-mode actuation in human–robot interaction applications," IEEE/ASME Trans. Mechatron., 14(1), 105-118.

[7] M. Zinn, B. Roth, O. Khatib, J. K. Salisbury, 2004, "A new actuation approach for human friendly robot design," Int. J. Robot. Res., 23(4-5), 379-398.

[8] R. V. Ham, T. Sugar, B. Vanderborght, K. Hollander, D. Lefeber, 2009, "Compliant actuator designs," IEEE Robot. Autom. Mag., 16(3), 81-94.

[9] C. Lagoda, A. C. Schouten, A. H. Stienen, E. E. Hekman, H. van der Kooij, 2010, "Design of an electric series elastic actuated joint for robotic gait rehabilitation training," IEEE RAS/EMBS Int. Conf. Biomedical Robotics and Biomechatronics, 21-26.

[10] G. Carpino, D. Accoto, F. Sergi, N. L. Tagliamonte, E. Guglielmelli, 2012, "A novel compact torsional spring for series elastic actuators for assistive wearable robots," ASME J. Mech. Des., 134, 121002.

[11] N. G. Tsagarakis, Z. Li, J. Saglia, D. G. Caldwell, 2011, "The design of the lower body of the compliant humanoid robot "cCub"", IEEE ICRA, 2035-2040.

[12] http://mekabot.com/products/compliant-arm/

[13] http://www.rethinkrobotics.com/

[14] C.-C. Lan, K.-M. Lee, 2006, "Generalized shooting method for analyzing compliant mechanisms with curved members," ASME J. Mech. Des., 128(4), 765-775.

[15] C.-C. Lan, Y.-J. Cheng, 2008, "Distributed shape optimization of compliant mechanisms using intrinsic functions," ASME J. Mech. Des., 130, 072304.

[16] M. Bodson, J. N. Chiasson, R. T. Novotnak, R. B. Rekowski, 1993, "High-performance nonlinear feedback control of a permanent magnet stepper motor," IEEE Trans. Control Syst. Tech., 1(1), 5-14.